JOURNAL OF GUIDANCE, CONTROL, AND DYNAMICS
Vol. 33, No. 6, November–December 2010

Specialized Coordinate Representation for Dynamic Modeling and Orbit Estimation of Geosynchronous Orbits

Jill Tombasco* and Penina Axelrad†
University of Colorado, Boulder, Colorado 80309
and
Moriba Jah‡
U.S. Air Force Research Laboratory, Kihei, Hawaii 96753

DOI: 10.2514/1.48903

This study investigates dynamic modeling and orbit estimation of geosynchronous satellites using traditional and specialized orbit representations. Exact nonlinear variational equations for generally perturbed synchronous elements are developed via Poisson brackets. A hybrid element set is also introduced to avoid numerical sensitivities. Numerical propagation studies evaluate the precision and accuracy of inertial Cartesian, Keplerian, synchronous, and hybrid element dynamic models. The suitability of approximating the synchronous element equations of motion for small eccentricity and inclination values is assessed. Results show that the hybrid and exact synchronous models are consistent for large and small time steps and are of comparable accuracy to the inertial Cartesian model. The hybrid element model is further validated via an estimation analysis that processes multiple nights of experimental optical data of the Tracking and Data Relay Satellite 8. The results show that the hybrid elements are suitable for geosynchronous dynamic modeling and estimation.

I. Introduction

OBJECTS placed in geostationary orbits appear fixed in an Earth-centered Earth-fixed frame and those in geosynchronous orbits exhibit diurnal oscillatory motion as seen from this reference frame. Because of this unique quality, the geosynchronous orbit regime contains numerous high-value military, scientific, and commercial satellites. The U.S. Strategic Command maintains element sets for all tracked resident space objects. Approximately 400 geosynchronous element sets are publicly available via the Space-Track[§] Web site managed by the U.S. Air Force. However, the ESA Database and Information System Characterizing Objects in Space system contains approximately 1040 catalogued objects that pass through the geosynchronous orbit. Of these 1040 objects, ≈350 objects are controlled active satellites, ≈150 objects are in libration orbits about the east–west stability points, and ≈400 uncontrolled objects are drifting in or near the geosynchronous orbit [1].

Specialized synchronous elements are defined by Soop [2] as a convenient representation of low-inclination, low-eccentricity, 24-hour-period orbits, which provide physical insight into the object motion. Conventional methods for orbit propagation and estimation use classical Keplerian elements or inertial position and velocity vectors to represent the state. Unfortunately, neither of these representations is ideal for the near-geosynchronous regime; classical orbit elements are poorly defined for near-zero eccentricity and inclination, and the rapidly changing inertial position and velocity coordinates obscure the simplicity and near-linearity of near-geosynchronous motions [3]. Equinoctial elements are comparable to the classical elements but are better suited to the low-inclination, low-eccentricity case; synchronous elements are a specialized set defined specifically for this orbit regime and provide physical insight into object motion in the geosynchronous region. This work explores the utility of synchronous elements and a hybrid set of equinoctial and synchronous elements for dynamical modeling and estimation of near-geosynchronous orbits.

This study investigates three primary topics: perturbation modeling for the synchronous and hybrid elements as compared to the Keplerian and Cartesian coordinates, approximations to the equations of motion for small eccentricity and inclination values, and the utility of the specialized elements in geosynchronous orbit estimation. An exact nonlinear synchronous element dynamic model is developed for arbitrary perturbations and approximated for small inclination and eccentricity. While similar models have been developed for long-term mean perturbed motion (on the order of years), this research models the short-period dynamics (on the order of several days) [4,5].

Batch estimation using experimental optical data is used to assess the feasibility of modeling realistic satellite dynamics with the specialized hybrid elements. A batch processor is developed to estimate the hybrid elements based on optical observations of azimuth and elevation. Multiple consecutive nights of optical data of TDRS 8 were provided by the U.S. Air Force Maui Optical and Supercomputer Site. Solutions are produced by processing two consecutive nights of data. The solutions are compared to a TDRS 8 multiday reference orbit and osculating element sets provided by the NASA Goddard Space Flight Center Flight Dynamics Facility (FDF). The osculating element sets are accurate to 30–40 m, while the multiday ephemerides are accurate to the kilometer level. The performance of the hybrid estimator in processing TDRS 8 data is compared to that of an inertial Cartesian state batch estimator.

The utility of the specialized element sets presented in this work is not limited to accurate dynamic modeling of geosynchronous dynamics. The synchronous and hybrid elements can also be applied to characterizing an object as an active satellite or space debris, as well as association of observations to a specific satellite. As these elements change very little in the geosynchronous regime, due to natural perturbations, they facilitate detection of incorrect data association or vehicle maneuvers.

Received 12 January 2010; revision received 7 July 2010; accepted for publication 12 July 2010.

*Graduate Student, Aerospace Engineering Sciences Department. Student Member AIAA.
†Professor, Aerospace Engineering Sciences Department. Fellow AIAA.
‡Director, Advanced Sciences and Technology Research Institute for Astrodynamics, Directed Energy Directorate. Professional Member AIAA.

§Data available online at http://www.space-track.org [retrieved 7 January 2010].

II. Development of Dynamic Model

The following section defines the synchronous element set and develops exact nonlinear variational equations for arbitrary orbit perturbations. Small inclination approximations are applied to the exact equations to simplify the dynamic model, and the resulting variational equations are linearized for the near-zero eccentricity geosynchronous condition.

A. Synchronous Elements

The synchronous elements are an approximated version of the equinoctial elements and are defined as the Earth-fixed subsatellite longitude λ, the longitudinal drift rate $\Delta\bar{a}$, eccentricity vector components (e_x, e_y), and the small-inclination approximated projection of the inclination vector onto the equatorial plane (i_x, i_y). The eccentricity and inclination vector components are depicted in Figs. 1a and 1b, respectively. The synchronous elements are defined in terms of the better-known semimajor axis a, eccentricity e, inclination i, right ascension of the ascending node Ω, argument of perigee ω, and true anomaly ν as follows [2]:

$$\lambda = (\omega + \Omega + \nu) - G(t) \tag{1a}$$

$$\Delta\bar{a} = \frac{a - A}{A} \tag{1b}$$

$$e_x = e\cos(\omega + \Omega) \tag{1c}$$

$$e_y = e\sin(\omega + \Omega) \tag{1d}$$

$$i_x = i\sin(\Omega) \tag{1e}$$

$$i_y = -i\cos(\Omega) \tag{1f}$$

$$s = \lambda + G(t) \tag{1g}$$

$$G(t) = G_0 + \omega_E(t - t_0) \tag{1h}$$

The spacecraft sidereal angle s is defined by Eq. (1g). Equation (1h) represents the Greenwich sidereal angle at a given time, ω_E denotes the average Earth rotation rate, and A denotes the nominal geosynchronous semimajor axis of 42,164.2 km for an Earth gravitational constant μ of 398, 600.440 km^3/s^2.

B. Exact Nonlinear Variational Equations

The method of Poisson brackets is employed to derive the exact variational equations for general perturbations. Poisson brackets relate the time rate of change of any orbital element x to the contribution of natural orbital motion and the contribution of disturbing accelerations $\mathbf{a}_D$. The time rate of change of an element as derived via Poisson brackets is given by [6]

$$\frac{\mathrm{d}x}{\mathrm{d}t} = \frac{\partial x}{\partial \mathbf{v}}\mathbf{a}_D + \frac{\partial x}{\partial t} \tag{2}$$

For verification, the differential equations are derived by taking the partial derivatives of Eqs. (1a–1f) with respect to time and the Keplerian elements. The Keplerian element time derivatives are substituted into the partial derivatives to produce exact nonlinear synchronous element variational equations. This method has been used previously to present synchronous element variational equations specific to the effect of perturbations on individual elements, such as the effect of lunisolar perturbations on inclination and solar pressure on eccentricity [7,8].

The full derivation of the exact nonlinear synchronous element variational equations via Poisson brackets is provided in the Appendix. To summarize, the resulting exact nonlinear synchronous element variational equations as functions of the body-fixed radial, tangential, and out-of-plane disturbing accelerations a_r, a_θ, and a_h are given by

$$\dot{\lambda} = \frac{h}{r^2} + \frac{r}{h}\tan\left(\frac{i}{2}\right)\sin(\omega + \nu)a_h - \omega_E \tag{3a}$$

$$\Delta\dot{\bar{a}} = \frac{2(\Delta\bar{a} + 1)^2}{hA}\left[(e_x\sin(s) - e_y\cos(s))a_r + \frac{p}{r}a_\theta\right] \tag{3b}$$

$$\dot{e}_x = \frac{r}{h}\left\{\frac{p}{r}\sin(s)a_r + \left[e_x + \left(1 + \frac{p}{r}\right)\cos(s)\right]a_\theta\right\} + e_y\frac{r}{h}\left\{\left[\tan\left(\frac{i}{2}\right)\sin(\Omega)\cos(s) - \tan\left(\frac{i}{2}\right)\cos(\Omega)\sin(s)\right]a_h\right\} \tag{3c}$$

$$\dot{e}_y = \frac{r}{h}\left\{\frac{-p}{r}\cos(s)a_r + \left[e_y + \left(1 + \frac{p}{r}\right)\sin(s)\right]a_\theta\right\} - e_x\frac{r}{h}\left\{\left[\tan\left(\frac{i}{2}\right)\sin(\Omega)\cos(s) - \tan\left(\frac{i}{2}\right)\cos(\Omega)\sin(s)\right]a_h\right\} \tag{3d}$$

$$\dot{i}_x = \left[\frac{r}{h}\sin(\Omega)\cos(\omega + \nu) + \frac{ir}{h\sin(i)}\cos(\Omega)\sin(\omega + \nu)\right]a_h \tag{3e}$$

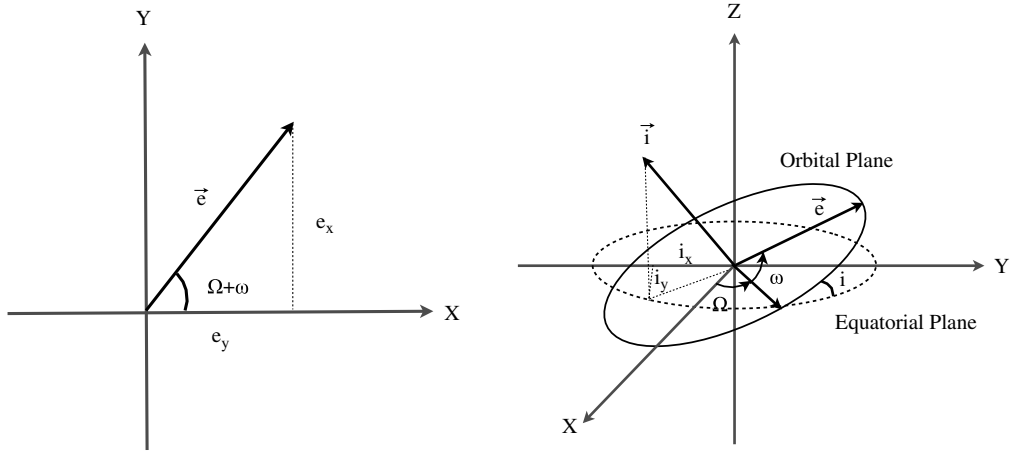

a) Eccentricity **b) Inclination**

Fig. 1 Eccentricity and inclination inertial vector components.

$$\dot{i}_y = \left[\frac{ir}{h\sin(i)}\sin(\Omega)\sin(\omega+\nu) - \frac{r}{h}\cos(\Omega)\cos(\omega+\nu)\right]a_h \tag{3f}$$

where r is the radial distance of the satellite from the center of the Earth, p is the semilatus rectum, and h is the angular momentum magnitude. Substituting the synchronous elements for the Keplerian elements in the orbit radius and semilatus rectum definitions [9] produces the orbital quantities in terms of the synchronous elements, as follows:

$$r = \frac{A(\Delta\bar{a}+1)(1-e_x^2-e_y^2)}{1+e_x\cos(s)+e_y\sin(s)} \tag{4a}$$

$$p = A(\Delta\bar{a}+1)(1-e_x^2-e_y^2) \tag{4b}$$

$$h = \sqrt{\mu p} \tag{4c}$$

Though the synchronous element variational equations are not truly singular, at very small inclination angles Eqs. (3e) and (3f) have the potential for numerical sensitivity.

C. Small Inclination Approximations

It is desirable to format the synchronous differential equations in a manner such that they provide physical insight into the effects of general perturbations. First, small-inclination approximations [$\sin(i) \approx \tan(i) \approx i$ and $\cos(i) \approx 1$] are applied to the exact equations. Applying the small-inclination approximations has the benefit of removing the potential for numerical sensitivity at near-zero inclination. The small-inclination approximated equations of motion are given by

$$\dot{\lambda} \approx \frac{h}{r^2} + \frac{r}{2h}[i_y\sin(s) + i_x\cos(s)]a_h - \omega_E \tag{5a}$$

$$\Delta\dot{\bar{a}} \approx \frac{2(\Delta\bar{a}+1)^2}{hA}\left[(e_x\sin(s) - e_y\cos(s))a_r + \frac{p}{r}a_\theta\right] \tag{5b}$$

$$\dot{e}_x \approx \frac{r}{h}\left\{\frac{p}{r}\sin(s)a_r + \left[e_x + \left(1+\frac{p}{r}\right)\cos(s)\right]a_\theta + \frac{e_y}{2}[i_x\cos(s) + i_y\sin(s)]a_h\right\} \tag{5c}$$

$$\dot{e}_y \approx \frac{r}{h}\left\{\frac{-p}{r}\cos(s)a_r + \left[e_y + \left(1+\frac{p}{r}\right)\sin(s)\right]a_\theta - \frac{e_x}{2}[i_x\cos(s) + i_y\sin(s)]a_h\right\} \tag{5d}$$

$$\dot{i}_x \approx \frac{r}{h}\sin(s)a_h \tag{5e}$$

$$\dot{i}_y \approx -\frac{r}{h}\cos(s)a_h \tag{5f}$$

D. Small-Eccentricity Linearization

The small-inclination variational equations are next linearized for near-zero eccentricity via a first-order Taylor series approximation about zero eccentricity. Near-zero eccentricity is a reasonable assumption for geosynchronous dynamic modeling. Taking the first variation of Eqs. (5a–5f) produces the following linearized equations, where n denotes the mean motion:

$$\dot{\lambda} \approx -\frac{1}{2}\sqrt{\frac{A(\Delta\bar{a}+1)}{\mu}}[i_y\sin(s) + i_x\cos(s)]a_h + (n-\omega_E) + 2n[e_x\cos(s) + e_y\sin(s)] \tag{6a}$$

$$\Delta\dot{\bar{a}} \approx \frac{2}{An}[1 + e_x\cos(s) + e_y\sin(s)]a_\theta + \frac{2}{An}[e_x\sin(s) - e_y\cos(s)]a_r \tag{6b}$$

$$\dot{e}_x \approx \sqrt{\frac{A(\Delta\bar{a}+1)}{\mu}}[\sin(s)a_r + (\cos(s)[2 - e_x\cos(s) - e_y\sin(s)] + e_x)a_\theta] \tag{6c}$$

$$\dot{e}_y \approx \sqrt{\frac{A(\Delta\bar{a}+1)}{\mu}}[-\cos(s)a_r + (\sin(s)[2 - e_x\cos(s) - e_y\sin(s)] + e_y)a_\theta] \tag{6d}$$

$$\dot{i}_x \approx \sqrt{\frac{A(\Delta\bar{a}+1)}{\mu}}[1 - e_x\cos(s) - e_y\sin(s)]\sin(s)a_h \tag{6e}$$

$$\dot{i}_y \approx \sqrt{\frac{A(\Delta\bar{a}+1)}{\mu}}[e_x\cos(s) + e_y\sin(s) - 1]\cos(s)a_h \tag{6f}$$

E. Hybrid Element Set

To circumvent the possibility of numerical issues when using an exact specialized dynamic model, the synchronous inclination terms can be replaced by the equinoctial elements Q_1 and Q_2 as given by

$$Q_1 = \tan\left(\frac{i}{2}\right)\sin(\Omega) \tag{7a}$$

$$Q_2 = \tan\left(\frac{i}{2}\right)\cos(\Omega) \tag{7b}$$

The specialized hybrid element set shown is now defined as

$$\mathbf{X} = [\lambda \quad \Delta\bar{a} \quad e_x \quad e_y \quad Q_1 \quad Q_2]^T \tag{7c}$$

The exact variational equations of this specialized hybrid element set are expressed as functions of Q_1 and Q_2 as follows:

$$\dot{\lambda} = \frac{h}{r^2} + \frac{r}{h}[Q_2\sin(s) - Q_1\cos(s)]a_h - \omega_E \tag{8a}$$

$$\Delta\dot{\bar{a}} = \frac{2(\Delta\bar{a}+1)^2}{hA}\left[(e_x\sin(s) - e_y\cos(s))a_r + \frac{p}{r}a_\theta\right] \tag{8b}$$

$$\dot{e}_x = \frac{r}{h}\left\{\frac{p}{r}\sin(s)a_r + \left[e_x + \left(1+\frac{p}{r}\right)\cos(s)\right]a_\theta + e_y[Q_1\cos(s) - Q_2\sin(s)]a_h\right\} \tag{8c}$$

$$\dot{e}_y = \frac{r}{h}\left\{\frac{-p}{r}\cos(s)a_r + \left[e_y + \left(1+\frac{p}{r}\right)\sin(s)\right]a_\theta - e_x[Q_1\cos(s) - Q_2\sin(s)]a_h\right\} \tag{8d}$$

$$\dot{Q}_1 = \frac{r}{2h}(1 + Q_1^2 + Q_2^2)\sin(s)a_h \tag{8e}$$

$$\dot{Q}_2 = \frac{r}{2h}(1 + Q_1^2 + Q_2^2)\cos(s)a_h \tag{8f}$$

The derivation of Eqs. (8e) and (8f) is presented in [6].

The equations of motion presented in this section have various advantages and disadvantages. The small-inclination approximated and small-eccentricity linearized synchronous element models are accurate to first order, but provide greater physical insight than the exact synchronous element model. For example, the approximated models clearly demonstrate that an out-of-plane disturbing acceleration will primarily induce oscillations in the orbit longitude and inclination. This perturbation will also introduce small oscillations to the eccentricity elements, but this effect is minor, as it is scaled by small eccentricity and inclination values. No variation in the longitudinal drift rate is induced by an out-of-plane perturbation. To verify these predicted results, a constant out-of-plane acceleration of 10^{-5} m/s^2 is applied to the exact synchronous element model, which is then numerically integrated for one day. Figure 2 shows the resulting synchronous elements over the one-day propagation. For comparison, the synchronous elements have been detrended by removing the mean elemental values, which are also shown in the figure, and have been individually scaled by the indicated amount. It is seen that the longitude and inclination terms are dominated by oscillatory behavior, while the eccentricity oscillations are at least 5 orders of magnitude smaller than the mean values. As expected, the drift rate shows no variation.

While the approximated models offer physical insight useful in predicting the effect of perturbations or maneuvers on orbital element variation, these models are hindered by the inherent second-order loss of accuracy. However, the hybrid element model is an exact representation of orbital motion that still provides perturbation insight useful for analytical prediction.

III. Analysis of General Perturbation Dynamic Model

It is necessary to analyze the applicability of synchronous and hybrid element dynamic modeling of geosynchronous motion under general perturbations. The model accuracy is tested by evaluating the consistency of propagations using different coordinate representations. The model precision is tested by assessing the propagation consistency when numerically integrating with both large and small fixed time steps.

A. Dynamic Model Accuracy Analysis

To analyze the accuracy of the equations of motion for the synchronous and hybrid elements, the synchronous propagation for a fixed time step of 60 s is compared to a reference propagation. The reference propagation is computed by numerically integrating inertial Cartesian elements with a variable-step fifth-order Runge–Kutta numerical integrator with an accuracy tolerance of 10^{-12} m and m/s. Fixed-step propagation of the inertial Cartesian, Keplerian, hybrid, exact synchronous, small-inclination approximated synchronous, and small-eccentricity linearized synchronous equation of motion are compared to the variable-step reference propagation.

The initial conditions and physical satellite parameters shown in Table 1, identical for each propagation, are taken from the TDRS 8 osculating element set for 2 July 2005.[¶] The satellite physical characteristics include the spacecraft surface area and mass and the reflectivity C_r. A fifth-order Runge–Kutta fixed-step integrator is chosen to provide a direct comparison among the coordinate representation propagations. The integrated equations of motion include two-body dynamics, Earth oblateness, lunisolar gravity, and solar pressure perturbations. The solar pressure acceleration is modeled assuming that the satellite is spherical and that no solar pressure perturbation acts on the satellite when it is shadowed by the Earth.

[¶]Data available online from https://wakata.nascom.nasa.gov// [retrieved 11 September 2009].

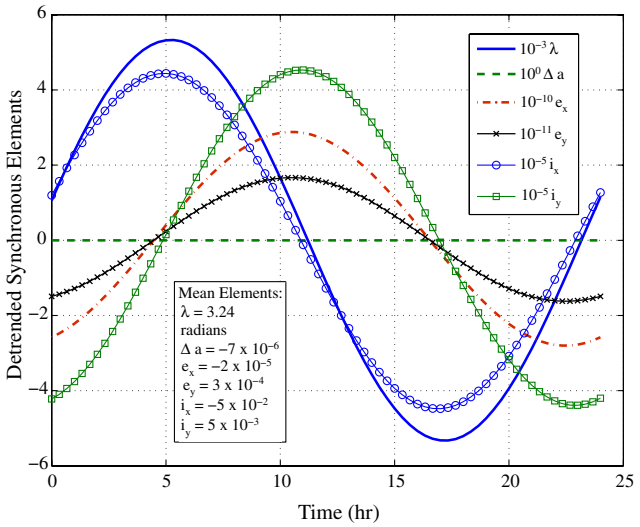

Fig. 2 Variation in synchronous elements because of a constant out-of-plane perturbation.

Figure 3 displays the differences between each propagation and the reference propagation. The inertial Cartesian, Keplerian, exact synchronous, and hybrid propagations are nearly identical. The errors of each propagation are on the order of 10^{-7} to 10^{-6} m in position and 10^{-11} to 10^{-10} m/s in velocity. The error consistency indicates that the exact nonlinear synchronous element and hybrid element dynamic models are as accurate as the more traditional Keplerian and inertial position and velocity dynamic models. Furthermore, the small errors from the reference orbit indicate that a 60 s time step is appropriate for fixed-step numerical propagation of geosynchronous orbits.

Figure 3 also presents the propagation error for the small-inclination synchronous model. The small-inclination propagation errors are approximately 10^{-4} to 1 m in position and 10^{-9} to 10^{-5} m/s in velocity. The initial inclination for this simulation is approximately 2.5 deg. Additional studies are performed in which the initial inclination is decreased by one order of magnitude, which produces propagation error on the same order of magnitude as the exact synchronous elements. Of the current Space-Track database, approximately 70% of the geosynchronous satellites currently tracked possess inclinations of 1 deg or smaller (see footnote [§]).

B. Dynamic Model Precision Analysis

The integration time step for geosynchronous propagation should be carefully chosen, as time steps that are too large lose dynamic fidelity, while time steps that are too small may accumulate errors, due to limited numerical precision in the case of small perturbations. The dynamics of a geosynchronous object are such that a set of elements that changes slowly over time is better suited for modeling than an element set that changes more dynamically. With an appropriate element set, long integration time steps adequately capture the motion.

Table 1 Simulation initial conditions and satellite characteristics

Parameter	Value
Epoch	2 July 2005 0:0:0 UTC
a	42,163.9203 km
e	0.00027562
i	2.6491°
Ω	263.9230°
ω	189.3889°
M	12.5343°
Area	65.65 m^2
Mass	1733.4973 kg
C_r	1.38251

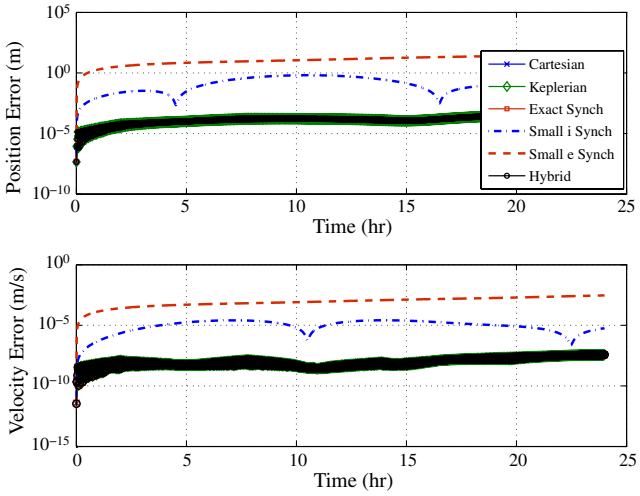

Fig. 3 Error relative to reference propagation.

The precision study is conducted by integrating a set of initial conditions four separate times, each with a different integration time step. The time steps chosen for this study are 1, 6, 60, and 600 s. Inertial Cartesian, Keplerian, exact synchronous and hybrid elements are propagated via a fixed-step numerical integrator for each of the time steps listed. The differences between the propagated orbits of a given element set are a direct measure of the integration consistency. All propagated state differences are expressed in inertial Cartesian coordinates for comparison. For each coordinate representation, the 1, 6, and 600 s fixed time-step propagations are differenced from the 60 s propagation.

A dynamic model that is not sensitive to time-step size is clearly preferable for computational purposes. It is expected that the Cartesian model will be sensitive to the time step, as the elements are very large compared to their dynamic changes. The synchronous, hybrid, and Keplerian models are not expected to exhibit either inconsistent or increasing propagation error. The initial conditions, shown in Table 1, have been chosen such that the Keplerian equations of motion will not encounter singularities.

First, the inertial Cartesian model precision is analyzed. Figure 4 presents the 1, 6, and 600 s inertial Cartesian position and velocity propagations, respectively, differenced from the 60 s propagation. The figure shows that the differences change by orders of magnitude, indicating that the Cartesian propagation is not very consistent as the step size is increased from 1 to 600 s. The 600 s propagation shows the largest error, on the order of 10^{-2} m and 10^{-6} m/s. The error of the 1 s propagation (10^{-7} to 10^{-5} m in position, 10^{-11} to 10^{-10} m/s in velocity) compared to that of the 6 s propagation (10^{-8} to 10^{-6} m in position, 10^{-12} to 10^{-11} m/s in velocity) indicates that the Cartesian integrator encounters numerical issues when the time step is too small. This is likely because the elemental variations due to perturbations are small in comparison to the dominant two-body dynamics for a geosynchronous satellite. This causes the perturbation effects to be lost through limited numerical precision.

Figure 5 displays the propagation errors for the Keplerian precision analysis. The propagation differences are on the order of 10^{-7} to 10^{-5} m in position and 10^{-11} to 10^{-9} m/s in velocity for all cases, showing that the Keplerian model is less dependent on time-step size than the Cartesian model. Again, the 1 s time step presents the largest error, indicating that numerical issues may exist at smaller integration steps. An additional study, in which the initial eccentricity is decreased by one order of magnitude and the precision analysis repeated, investigates the Keplerian element modeling of a satellite in a less eccentric orbit. The propagation errors are shown in Fig. 6. The results show that for large time steps (600 s) near-zero eccentricity values produce offsets and discontinuities in the propagation differences, due to the singularities of the Keplerian element equations of motion.

The 1, 60, and 600 s fixed time-step propagation errors for the exact synchronous element model are shown in Fig. 7. The differences are consistent on the order of 10^{-7} to 10^{-6} m in position and 10^{-11} to 10^{-10} m/s in velocity. This result is expected, as the

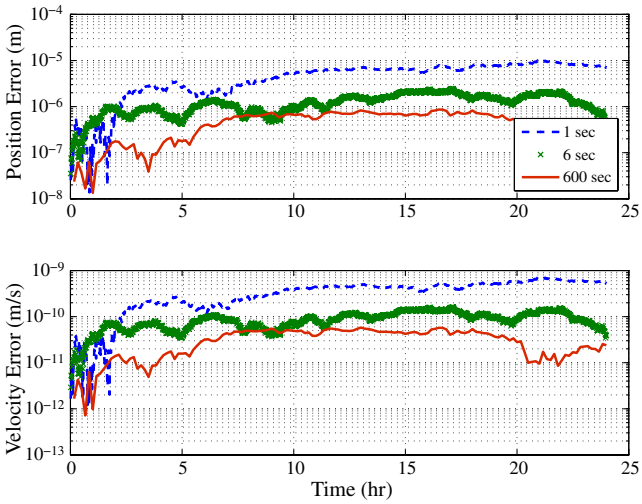

Fig. 5 Keplerian model error relative to 60 s fixed time-step propagation.

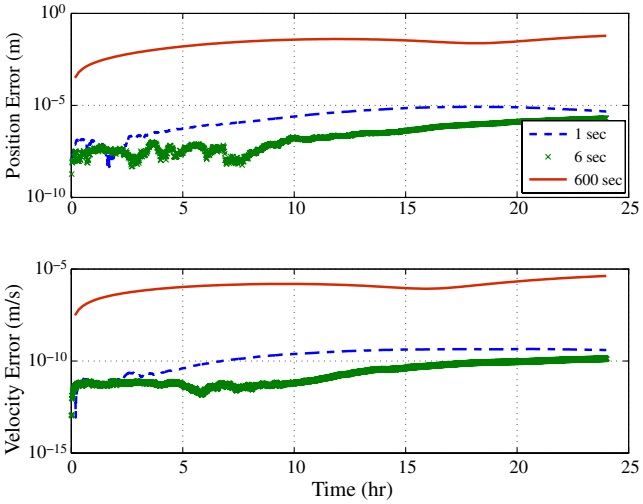

Fig. 4 Inertial Cartesian model error relative to 60 s fixed time-step propagation.

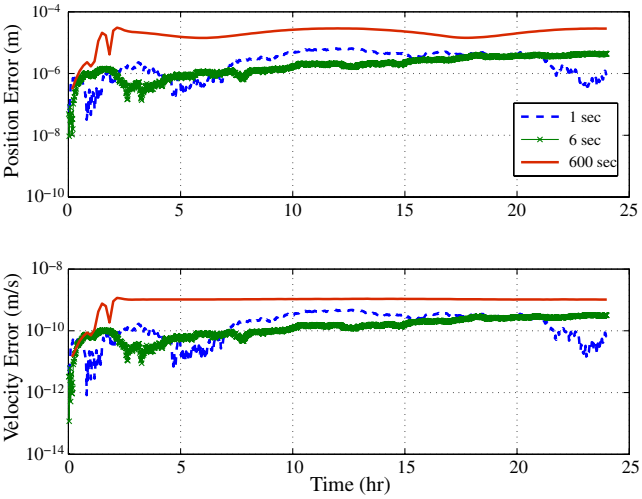

Fig. 6 Keplerian model error relative to 60 s fixed time-step propagation; near-zero eccentricity.

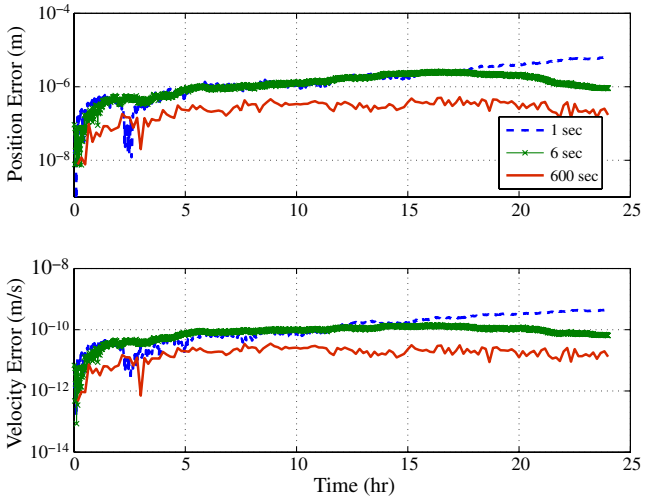

Fig. 7 Synchronous model error relative to 60 s fixed time-step propagation.

synchronous elements are designed to change by a small amount, and the singularity in the inclination component equations of motion is largely cancelled out for small inclinations. In contrast to the Cartesian and Keplerian studies, the 1 s propagation error is the same order of magnitude as the 6 s propagation error. However, the error grows slowly over time, indicating that there is still a numerical issue that arises with small time steps.

Figure 8 presents the errors of the 1, 6, and 600 s fixed time-step hybrid element propagation from the 60 s propagation. The results are similar to those of the synchronous element model; the position and velocity error is consistent to approximately one order of magnitude. The position error is approximately 10^{-6} to 10^{-7}, while the velocity error is approximately 10^{-11} to 10^{-10} m/s. As seen for the inertial Cartesian and Keplerian propagations, the hybrid element 1 s propagation error is slightly larger than that of the 6 and 600 s propagations.

C. Results of Dynamic Model Analysis

The numerical propagation study indicates that the time interval for a geosynchronous fixed-step fifth-order Runge–Kutta numerical integrator must be chosen with care, as time steps that are too small (1 s) or too large (600 s) may introduce numerical issues. It must be noted that the accuracy of a higher-order fixed-step numerical integrator will not be as sensitive to time-step size. Large time steps are suitable for synchronous and hybrid element propagation. Small integration time steps are computationally expensive and are not generally useful for geosynchronous orbit propagation.

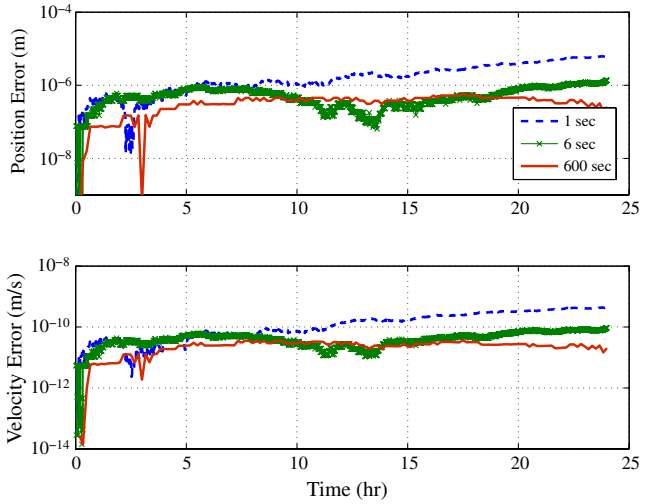

Fig. 8 Hybrid model error relative to 60 s fixed-time-step propagation.

Comparison of various element-set propagations reveals that the exact differential equations for the synchronous and hybrid elements are as accurate as Keplerian and Cartesian geosynchronous propagations. However, the small-inclination and eccentricity approximated synchronous equations of motion for the synchronous elements are not accurate enough for precise applications in which submeter accuracy is required. Given their simplicity, the approximated synchronous differential equations may be suitable for applications with loose accuracy requirements such as mission planning. Furthermore, the simplified dynamic model provides physical insight into the effect of general perturbations. Given that the exact synchronous equations necessary for high-accuracy dynamic modeling can suffer from numerical sensitivity, there is no added benefit in using the synchronous elements over the equinoctial elements.

Based on the results of the numerical propagation analysis, the hybrid set of synchronous and equinoctial elements is chosen to accurately model the dynamics while avoiding potential singularities. The specialized hybrid element set is defined in Eq. (7c).

IV. Estimation Analysis

The specialized hybrid element dynamic model is next validated via an estimation analysis in which a 60 s fixed-step numerical integration of the exact nonlinear dynamics [Eqs. (8a–8e)] is used to model the satellite motion. A batch processor is developed to estimate the hybrid state vector [Eq. (7c)] by processing multiple nights of experimental optical data of TDRS 8. The performance of the hybrid batch estimator is analyzed by comparison to a multiday reference orbit produced by the FDF as well as comparison to the FDF osculating element sets. An inertial Cartesian batch estimator with identical dynamic and measurement model parameters is also used to process the optical observations of TDRS 8.

A. Hybrid Element Batch Estimator Development

The batch estimator is developed for the hybrid elements by deriving the state transition matrix Φ, the measurement model $G(\mathbf{X}, t)$, and the measurement sensitivity matrix $\tilde{H}$. The state transition matrix is a linearized temporal mapping of the state vector and state uncertainty from time $k-1$ to time k and is computed by numerical integration. The time derivative of the state transition matrix is given by

$$\dot{\Phi}(t_k, t_{k-1}) = [A]\Phi(t_k, t_{k-1}) = \left[\frac{\partial \dot{\mathbf{X}}(t_k)}{\partial \mathbf{X}(t_k)}\right]\Phi(t_k, t_{k-1}) \tag{9}$$

where the $[A]$ matrix is the partial derivatives of the state time derivatives with respect to the states.

For this study, the state transition matrix is used only to propagate the state covariance matrix, P. Unlike inertial Cartesian perturbed motion, the time variation of perturbed hybrid elements is always small in comparison to the elements themselves. Thus, a two-body propagation model can be used in the state transition matrix, and the resulting $[A]$ matrix has nonzero elements only in the first row, as follows:

$$[A] = \begin{bmatrix} A_{11} & A_{12} & A_{13} & A_{14} & 0 & 0 \\ 0 & 0 & 0 & 0 & 0 & 0 \\ 0 & 0 & 0 & 0 & 0 & 0 \\ 0 & 0 & 0 & 0 & 0 & 0 \\ 0 & 0 & 0 & 0 & 0 & 0 \\ 0 & 0 & 0 & 0 & 0 & 0 \end{bmatrix} \tag{10a}$$

$$A_{11} = \frac{2h}{rp}[e_y \cos(s) - e_x \sin(s)] \tag{10b}$$

$$A_{12} = \frac{-3h}{2r^2(\Delta\bar{a} + 1)} \tag{10c}$$

$$A_{13} = \frac{h}{r^2 p}[3Ae_y(\Delta\bar{a} + 1) + 2r\sin(s)] \tag{10d}$$

$$A_{14} = \frac{h}{r^2 p}[3Ae_x(\Delta\bar{a} + 1) + 2r\cos(s)] \tag{10e}$$

For the batch estimator dynamic model, the state vector is propagated via numerical integration of the exact nonlinear variational equations (8a–8f). The two-body state transition matrix is used for propagation of the covariance matrix from time $k-1$ to time k as follows:

$$P_k = \Phi(t_k, t_{k-1})P_{k-1}\Phi(t_k, t_{k-1})^T \tag{11}$$

This approach is numerically validated by comparing a one-day covariance propagation via the simplified state transition matrix with a nonlinear sigma-point propagation [10]. The two covariance matrices are compared via the size and orientation of each matrix.

The eigenvalue decomposition of both propagated covariance matrices are shown in Table 2, where e_k $(k = 1, \ldots, 6)$ denotes the principal components. The similarity of the matrix eigenvalues shows that the uncertainty scale is similar. The principal directions of the covariance matrices are compared by vector multiplication of corresponding eigenvectors; a value of ± 1 indicates that the principal axes are coaligned. Table 2 displays the results of the eigenvector multiplication, showing that the two covariance matrices are nearly aligned in orientation, with the strongest orientation alignment corresponding to the maximum eigenvalue. The results of the eigenvalue decomposition show that propagating the covariance matrix via a simple two-body dynamic model captures the realistic uncertainty scale and orientation of a nonlinear fully perturbed dynamic model.

To continue the batch estimator development, azimuth β and elevation ε angular measurements of satellite position are modeled. The measurement model $G(\mathbf{X}, t)$ is generated by expressing the Earth-centered/Earth-fixed (ECEF) position of the satellite as a function of the hybrid elements as given by

$$\mathbf{R}_{\text{ECEF}} = \begin{bmatrix} R_x \\ R_y \\ R_z \end{bmatrix} = [T^{\text{ECI}}_{\text{ECEF}}]\mathbf{R}_{\text{ECI}} = [T^{\text{ECI}}_{\text{ECEF}}]\frac{r}{1 + Q_1^2 + Q_2^2} \times \begin{bmatrix} (1 + Q_2^2 - Q_1^2)\cos(s) + 2Q_1Q_2\sin(s) \\ (1 + Q_1^2 - Q_2^2)\sin(s) + 2Q_1Q_2\cos(s) \\ 2(Q_2\sin(s) - Q_1\cos(s)) \end{bmatrix} \tag{12}$$

The ECEF position vector is then rotated into a topocentric frame and the measurement angles are geometrically computed. $T^{\text{ECEF}}_{\text{ECI}}$ denotes the transformation matrix from the Earth-centered inertial (ECI) frame to the ECEF frame, including precession, nutation, and nonconstant Earth rotation rate. $T^{\text{ENU}}_{\text{ECEF}}$ represents the geometric rotation from the ECEF frame to the east–north–up topocentric frame:

$$\boldsymbol{\rho}_{\text{ENU}} = \begin{bmatrix} \rho_E \\ \rho_N \\ \rho_U \end{bmatrix} = [T^{\text{ECEF}}_{\text{ENU}}](\mathbf{R}_{\text{ECEF}} - \mathbf{R}_{\text{site,ECEF}}) \tag{13}$$

Table 2 Eigenvalue decomposition of the propagated covariance matrices

Principal component	Two-body eigenvalue	Sigma-point eigenvalue	Eigenvector dot product
e_1	5.5×10^{-8}	5.3×10^{-8}	0.98
e_2	6.5×10^{-8}	5.6×10^{-8}	0.98
e_3	1.3×10^{-7}	1.3×10^{-7}	−0.99
e_4	7.0×10^{-5}	7.0×10^{-5}	−0.72
e_5	7.6×10^{-5}	8.0×10^{-5}	0.72
e_6	1.3×10^{-3}	1.2×10^{-3}	0.99

$$G(\mathbf{X}, t) = \begin{bmatrix} \beta \\ \varepsilon \end{bmatrix} = \begin{bmatrix} \tan^{-1}\left(\frac{\rho_E}{\rho_N}\right) & \sin^{-1}\left(\frac{\rho_U}{|\boldsymbol{\rho}_{\text{ENU}}|}\right) \end{bmatrix}^T \tag{14}$$

The measurement model includes normally distributed random noise with a mean of zero arcseconds and standard deviation of two arcseconds. Measurement corrections to account for the light transit time from the satellite to the ground-based sensor are also incorporated in the model. The measurement model does not account for aberration of the optical signal.

Finally, the measurement sensitivity matrix $\tilde{H}$ is determined by evaluating the partial derivatives of the measurement model with respect to the hybrid elements. For simplicity, the measurement sensitivity matrix is separated into its partial derivative components as follows:

$$\tilde{H} = \frac{\partial G(\mathbf{X}, t)}{\partial \boldsymbol{\rho}_{\text{ENU}}}\frac{\partial \boldsymbol{\rho}_{\text{ENU}}}{\partial \mathbf{R}_{\text{ECEF}}}\frac{\partial \mathbf{R}_{\text{ECEF}}}{\partial \mathbf{X}} \tag{15}$$

The partial derivative components are given by

$$\frac{\partial G(\mathbf{X}, t)}{\partial \boldsymbol{\rho}_{\text{ENU}}} = \begin{bmatrix} \left[\rho_N\left(\frac{\rho_E^2}{\rho_N^2} + 1\right)\right]^{-1} & -\rho_E\left[\rho_N\left(\frac{\rho_E^2}{\rho_N^2} + 1\right)\right]^{-1} & 0 \\ \frac{-\rho_E\rho_N}{\rho^2\sqrt{\rho^2 - \rho_U^2}} & \frac{-\rho_U\rho_N}{\rho^2\sqrt{\rho^2 - \rho_U^2}} & \frac{\sqrt{\rho^2 - \rho_U^2}}{\rho^2} \end{bmatrix} \tag{16}$$

$$\frac{\partial \boldsymbol{\rho}_{\text{ENU}}}{\partial \mathbf{R}_{\text{ECEF}}} = [T^{\text{ECEF}}_{\text{ENU}}]\frac{\partial(\mathbf{R}_{\text{ECEF}} - \mathbf{R}_{\text{site,ECEF}})}{\partial \mathbf{R}_{\text{ECEF}}} = [T^{\text{ECEF}}_{\text{ENU}}] \tag{17}$$

$$\frac{\partial \mathbf{R}_{\text{ECEF}}}{\partial \mathbf{X}} = [T^{\text{ECI}}_{\text{ECEF}}]\frac{\partial \mathbf{R}_{\text{ECI}}}{\partial \mathbf{X}} \tag{18}$$

The performance of the hybrid batch estimator is compared against the more conventional inertial Cartesian batch estimator. To ensure an appropriate comparison, the dynamic model is identical between both estimators. As was demonstrated in Sec. III.A and Fig. 3, at a 60 s fixed time step the numerical propagation in hybrid and inertial Cartesian state spaces is comparable.

It is anticipated that the inertial Cartesian batch estimator will not perform as well as the hybrid element batch estimator, due to the linearization of the measurement sensitivity matrix H. For a geosynchronous object the longitudinal state λ is highly correlated with the azimuthal angle measurement, whereas the ECI positions X and Y are position vector components primarily in the azimuth plane. Because of this nondirect relationship between X and Y and the azimuth measurement, the linearized inertial Cartesian measurement sensitivity matrix is more affected by a loss of second-order terms than the hybrid element measurement sensitivity matrix. This inaccuracy of the inertial Cartesian measurement sensitivity matrix will manifest as a poor longitudinal estimate and larger estimated state uncertainty when compared to that of the hybrid batch estimator.

B. Batch Estimator Results

The hybrid element batch estimator is validated by processing multiple nights of ground-based optical observations of TDRS 8. The estimator uses a reduced dynamic model including a 4×4 Earth gravity field, lunisolar gravity perturbations, and solar radiation pressure. TDRS 8 is chosen as a reference satellite, because the FDF computes and publishes daily high-accuracy osculating elements (30–40 m accuracy) as well as multiday long-term ephemerides (kilometer-level accuracy) for this satellite. The spacecraft parameters provided in the osculating element sets are used to model the solar pressure perturbation. From 2 July 2005 to 8 July 2005, six nights of TDRS 8 optical data were provided by the U.S. Air Force Maui Optical and Supercomputing Site. During the observation time period, FDF has verified maneuvers on the first and fifth days. To avoid data reduction over maneuvers, only the second through fourth and sixth through eighth nights of data are used in this analysis.

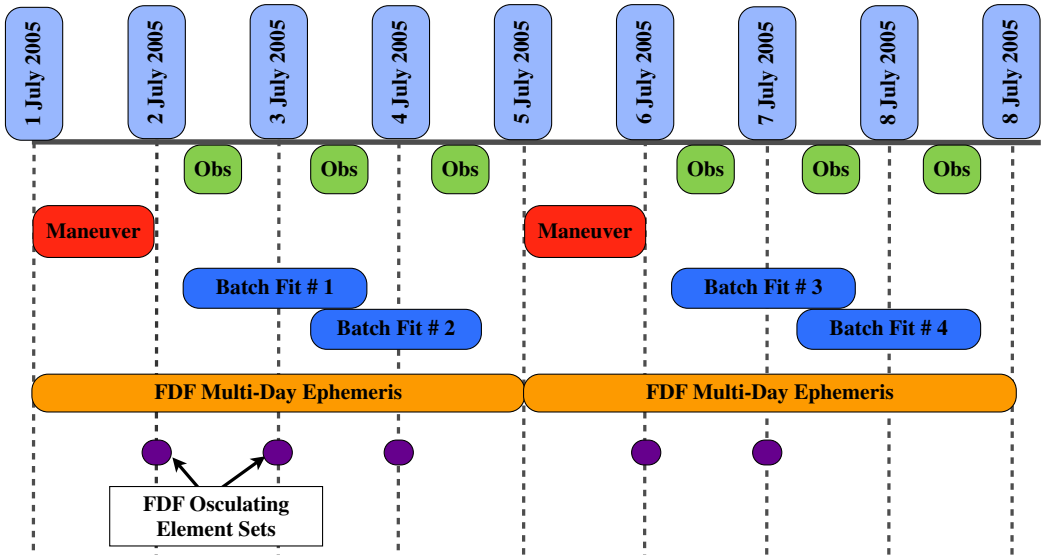

Fig. 9 Graphical representation of batch analysis timeline.

Throughout the data period, two consecutive nights of optical data are processed by the hybrid and inertial Cartesian estimators. The following data sets are processed: 2 July and 3 July (fit 1), 3 July and 4 July (fit 2), 6 July and 7 July (fit 3), and 7 July and 8 July (fit 4). A pictorial summary of the analysis timeline is shown in Fig. 9.

Table 3 Initial conditions for fit 1

Parameter	Value
λ	3.239042 rad
$\Delta\bar{a}$	2.0×10^{-6}
e_x	2.03×10^{-4}
e_y	-6.17×10^{-5}
Q_1	-2.2723×10^{-2}
Q_1	-2.496×10^{-3}
X	−38, 607.028 km
Y	−16, 870.673 km
Z	−1671.236 km
V_x	1.227676 km/s
V_y	−2.817972 km/s
V_z	0.069896 km/s

First, the impact of using the simplified two-body state transition matrix for uncertainty propagation is revisited and further analyzed by using two batch estimators to process the 2 July 2005 and 3 July 2005 data and comparing the hybrid state solutions. The first batch estimator uses the two-body state transition matrix while the second batch estimator uses a fully perturbed state transition matrix. All initial conditions and dynamic model parameters are identical for both estimations. The difference between the two solutions is on the order of millimeters in inertial position and micrometers per second in inertial velocity, indicating that use of the simplified state transition matrix does not significantly affect the estimator solution accuracy.

Several metrics are generated to test the hybrid and inertial Cartesian estimates. The error between the postfit solution and the multiday reference ephemeris is computed for both state-space solutions to each of the four batch fits. As the osculating elements are more accurate than the multiday reference ephemeris, the batch solution is propagated forward and backward to the available osculating element sets directly before and after the solution epoch. The error between the propagated solution and osculating elements is transformed into the radial, in-track, cross-track (RIC) reference frame. Finally, postfit residuals are compared with predicted

Table 4 Initial conditions for fits 2 through 4

	X	Y	Z	V_x	V_y	V_z
Fit 2	−39, 502.150 km	−14, 638.188 km	−1720.661 km	1.065057 km/s	−2.883369 km/s	0.062724 km/s
Fit 3	−36, 211.215 km	−21, 560.852 km	−1527.459 km	1.568735 km/s	−2.642071 km/s	0.084087 km/s
Fit 4	−31, 578.943 km	−12, 923.965 km	−1282.913 km	2.032161 km/s	−2.303849 km/s	0.103245 km/s

Table 5 Solution for fit 1

	X	Y	Z	V_x	V_y	V_z
Fit 1						
Hybrid	−38, 579.232 km	−16, 934.479 km	−1669.699 km	1.232320 km/s	−2.815933 km/s	0.070114 km/s
Cartesian	−38, 579.383 km	−16, 934.135 km	−1669.608 km	1.232295 km/s	−2.815944 km/s	0.070113 km/s
Fit 2						
Hybrid	−39, 504.664 km	−14, 638.772 km	−1720.748 km	1.065095 km/s	−2.883537 km/s	0.062746 km/s
Cartesian	−39, 504.775 km	−14, 638.390 km	−1720.752 km	1.065068 km/s	−2.883550 km/s	0.062744 km/s
Fit 3						
Hybrid	−36, 213.514 km	−21, 561.988 km	−1527.471 km	1.568815 km/s	−2.642234 km/s	0.084108 km/s
Cartesian	−36, 213.654 km	−21, 561.587 km	−1527.471 km	1.568789 km/s	−2.642257 km/s	0.084108 km/s
Fit 4						
Hybrid	−31, 580.609 km	−27, 925.193 km	−1282.885 km	2.032249 km/s	−2.303969 km/s	0.103265 km/s
Cartesian	−31, 580.843 km	−27, 924.889 km	−1282.893 km	2.032228 km/s	−2.303990 km/s	0.103265 km/s

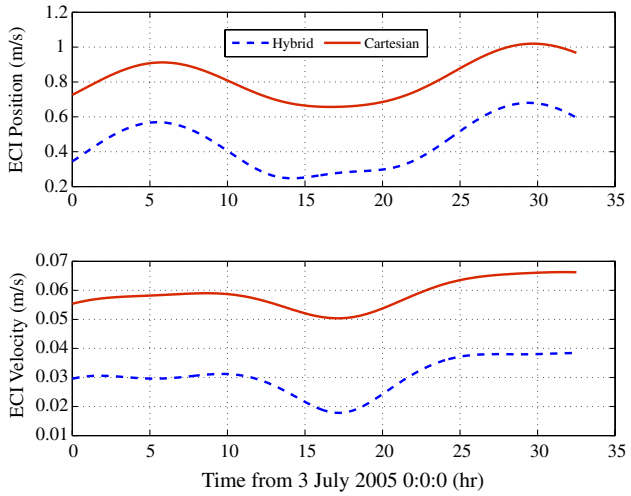

Fig. 10 Postfit solution error relative to multiday reference orbit.

residuals for the reference orbit. These metrics serve to evaluate the utility of hybrid element orbit estimation and compare the hybrid element batch performance with inertial Cartesian estimation.

The a priori satellite state for both the hybrid and inertial Cartesian batch estimators is initialized with the FDF multiday ephemeris interpolated at the observation epoch of each fit. The a priori ephemeris for fit 1 is shown in Table 3 in hybrid elements and inertial Cartesian coordinates. The initial conditions of fits 2 through 4 are shown in inertial Cartesian coordinates in Table 4. The hybrid and inertial Cartesian batch solutions for fits 1 through 4, also shown in inertial Cartesian coordinates, are presented in Table 5.

The fit 2 hybrid and Cartesian postfit solutions are, respectively, differenced from the FDF multiday reference orbit. Figure 10 shows the inertial position and velocity error magnitudes and is representative of the error magnitudes for fits 1, 3, and 4. The hybrid solution position and velocity errors are on the order of 600 m and 3 cm/s, respectively. The inertial Cartesian errors are on the order of 1 km in position and 7 cm/s in velocity. As both estimators employ identical dynamic parameters and initial conditions and the dynamic propagations are of comparable accuracy, the error differences shown in Fig. 10 demonstrate that the two state-space estimators converge on significantly different solutions. As the multiday reference orbit is only accurate to the kilometer level and both position error magnitudes are less than 1 km, conclusions cannot be drawn about the accuracy of each batch fit.

As the osculating elements are more accurate than the multiday ephemerides, the fit 1 solutions are also propagated back to the previous osculating element epoch [3 July 2005 0:0:0 UTC (Coordinated Universal Time)] and forward to the next available osculating element epoch (4 July 2005 0:0:0 UTC). Table 6 displays the difference between the propagated solutions and the FDF osculating element sets in the RIC position and velocity. Tables 7–9 present the RIC frame errors from the osculating element sets for fits 2, 3, and 4. The solution for fit 4 is only compared to the previous osculating element set as a high-accuracy osculating element set for

Table 6 Comparison of fit 1 solutions to FDF osculating elements

	R	I	C	V_r	V_i	V_c
0:0:0 UTC 2 July 2005						
Hybrid	10.110 m	−203.985 m	−227.187 m	1.0 cm/s	0.7 cm/s	−0.3 cm/s
Cartesian	10.666 m	−579.404 m	−227.214 m	3.7 cm/s	0.7 cm/s	−0.4 cm/s
0:0:0 UTC 3 July 2005						
Hybrid	6.603 m	−131.226 m	−228.759 m	1.3 cm/s	−0.1 cm/s	−0.1 cm/s
Cartesian	7.157 m	−506.651 m	−228.786 m	4.0 cm/s	−0.1 cm/s	−0.1 cm/s

Table 7 Comparison of fit 2 solutions to FDF osculating elements

	R	I	C	V_r	V_i	V_c
0:0:0 UTC 3 July 2005						
Hybrid	59.403 m	0.075 m	−215.707 m	−0.4 cm/s	0.1 cm/s	−0.6 cm/s
Cartesian	45.840 m	−484.717 m	−216.407 m	2.8 cm/s	0.3 cm/s	−0.5 cm/s
0:0:0 UTC 4 July 2005						
Hybrid	22.378 m	31.678 m	−246.666 m	0.4 cm/s	−0.1 cm/s	0 cm/s
Cartesian	8.321 m	−441.992 m	−247.307 m	3.7 cm/s	−0.1 cm/s	0 cm/s

Table 8 Comparison of fit 3 solutions to FDF osculating elements

	R	I	C	V_r	V_i	V_c
0:0:0 UTC 6 July 2005						
Hybrid	84.296 m	−114.922 m	−182.363 m	0.0 cm/s	−0.8 cm/s	0.1 cm/s
Cartesian	57.628 m	−805.466 m	−184.911 m	4.3 cm/s	−0.7 cm/s	0.1 cm/s
0:0:0 UTC 7 July 2005						
Hybrid	−21.582 m	−149.947 m	−220.089 m	1.0 cm/s	0.1 cm/s	0.4 cm/s
Cartesian	−49.825 m	−855.204 m	−222.514 m	5.8 cm/s	0.3 cm/s	0.4 cm/s

Table 9 Comparison of fit 4 solutions to FDF osculating elements at 0:0:0 UTC 7 July 2005

	R	I	C	V_r	V_i	V_c
Hybrid	133.173 m	−71.469 m	−179.006 m	−0.3 cm/s	−1.5 cm/s	0.0 cm/s
Cartesian	122.717 m	−559.841 m	−180.112 m	3.0 cm/s	−1.4 cm/s	0.01 cm/s

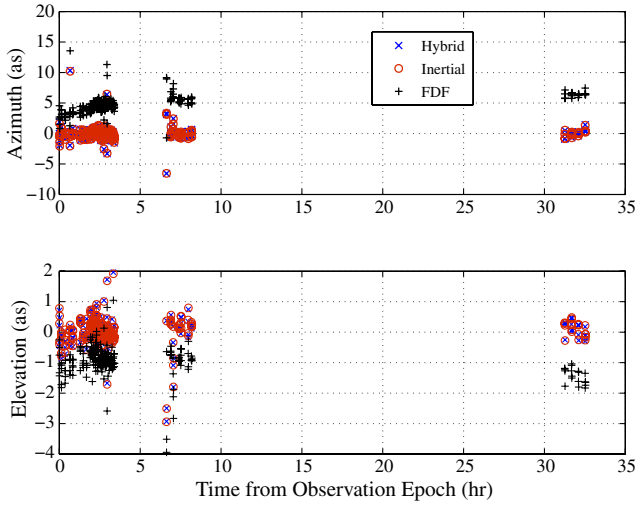

Fig. 11 Measurement residuals of multiday reference orbit and batch solutions.

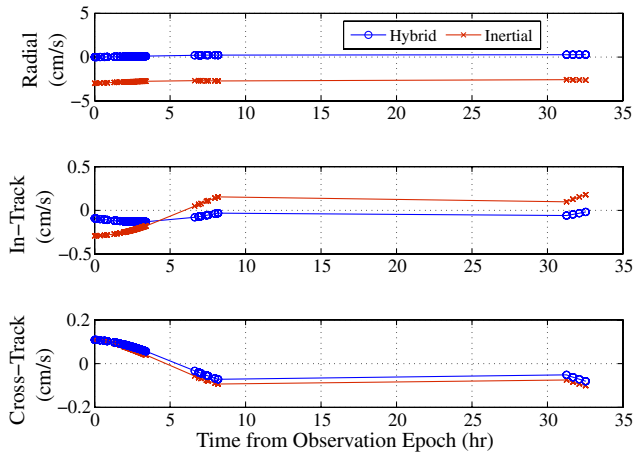

Fig. 12 Postfit RIC position error from simulated reference orbit.

8 July is not available. Each case shows that the hybrid element batch performs considerably better than the inertial Cartesian batch in estimating in-track position and radial velocity.

The postfit residuals for fit 2 are compared to residuals generated using the multiday reference ephemerides in order to assess how well each orbit fits the experimental data. The reference orbit is interpolated at the observations times. Figure 11 displays the residuals for the three days of measurements and is representative of each fit's results. The residual rms values are approximately 0.7 arcseconds in right ascension and 0.4 arcseconds in declination for all four fits. The systematic error seen in the hybrid estimator residuals is due to unmodeled solar pressure. The reference residuals do not display such systematic behavior; however, there is evidence of measurement bias. The right ascension reference residuals possess a time-varying offset, and there is a constant offset of approximately 1 arcsecond in declination. These offsets indicate sensor bias that

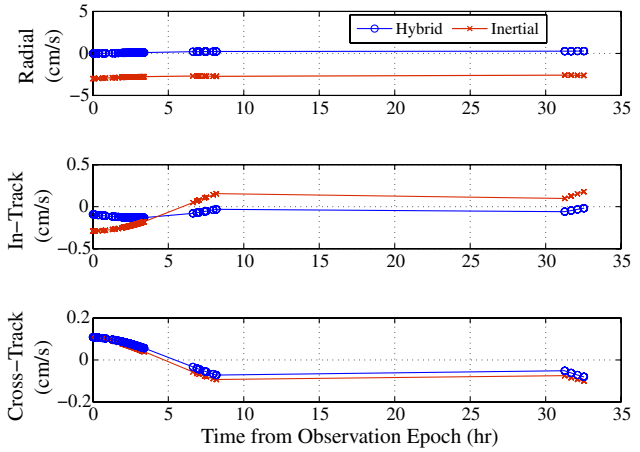

Fig. 13 Postfit RIC velocity error from simulated reference orbit.

may alias error into the batch solution. Note that 1 arcsecond is approximately 200 m at the geosynchronous altitude and may largely account for the batch solution position error.

The presence of systematic measurement error as well as unmodeled dynamics leads to the necessity to compare the hybrid element and inertial Cartesian batch estimators by processing simulated data. Simulated data are created to mimic the data sets of fits 1 and 2. A variable-step numerical propagator is initialized with the FDF osculating element sets for 2 July and 3 July, respectively. The dynamic model includes the 4×4 gravity field, lunisolar gravity, and solar radiation pressure. The simulated reference orbit is used to compute azimuth and elevation measurements at the same times as the experimental observations. The simulated observations are degraded with 2 arcseconds of Gaussian noise.

The hybrid and inertial Cartesian estimators, which now include perfect measurement and dynamic models, are initialized with the FDF multiday reference orbit interpolated to the observation epoch. The postfit solutions of each batch estimator are then differenced from the simulated reference orbit. Figures 12 and 13 present the RIC frame position and velocity errors relative to the reference orbit for the fit to simulated 3 July and 4 July data (experimental data fit 2). The simulation of fit 1 produces similar results. The results show that the radial and cross-track positions and in-track and cross-track velocity errors are the same order of magnitude for both estimators, indicating that the hybrid and batch are able to similarly recover these components. However, the in-track position and radial velocity errors are orders of magnitude larger for the inertial Cartesian estimator. The significant discrepancy in estimated solutions cannot be attributed to dynamic or measurement mismodeling or accuracies of the reference orbit; the inertial Cartesian estimator cannot recover the azimuthal motion as well as the hybrid element estimator, due to the linearization of the measurement sensitivity matrix.

To assess the impact of the measurement sensitivity matrix linearization on the estimation solution, the estimated state uncertainties are compared for the inertial Cartesian and hybrid element estimators. The estimated state uncertainties for the simulation of experimental data fit 1 and 2 are shown in hybrid element space in Table 10 and in ECI space in Table 11. The results show that the λ estimated uncertainty is one order of magnitude larger for the inertial Cartesian estimator than the hybrid estimator; all other hybrid

Table 10 Estimated hybrid state uncertainties of simulation analysis

	λ	$\Delta\bar{a}$	P_1	P_2	Q_1	Q_2
Fit 1						
Hybrid	1.12×10^{-6} rad	8×10^{-8}	3.6×10^{-7}	1.07×10^{-6}	3.7×10^{-7}	2.9×10^{-7}
Cartesian	2.436×10^{-5} rad	8×10^{-8}	5.9×10^{-7}	9.6×10^{-7}	3.8×10^{-7}	2.9×10^{-7}
Fit 2						
Hybrid	1.15×10^{-6} rad	1.7×10^{-7}	5.6×10^{-7}	1.25×10^{-6}	4.2×10^{-7}	3.5×10^{-7}
Cartesian	2.900×10^{-5} rad	1.7×10^{-7}	1.13×10^{-6}	7.8×10^{-7}	34.2×10^{-7}	2.9×10^{-7}

Table 11 Estimated ECI state uncertainties of simulation analysis

	X	Y	Z	V_x	V_y	V_z
Fit 1						
Hybrid	26.763 m	53.434 m	27.131 m	0.3 cm/s	0.4 cm/s	0.2 cm/s
Cartesian	26.808 m	56.485 m	27.129 m	0.3 cm/s	0.4 cm/s	0.2 cm/s
Fit 2						
Hybrid	33.750 m	60.691 m	31.334 m	0.3 cm/s	0.5 cm/s	0.3 cm/s
Cartesian	33.766 m	60.721 m	31.336 m	0.3 cm/s	0.5 cm/s	0.3 cm/s

element uncertainties are very similar. At the nominal geosynchronous altitude, the difference between the estimated longitudinal uncertainty is approximately 1 km. However, this significant longitudinal uncertainty difference is not visible in the ECI-space uncertainty, for which all state uncertainties are similar for both estimators.

V. Conclusions

This work analyzes the applicability of geosynchronous dynamic modeling with the specialized synchronous and hybrid elements as compared to more traditional Keplerian and inertial Cartesian coordinate representations. The specialized synchronous dynamic model for arbitrary perturbations is presented, as well as small-inclination and small-eccentricity approximated models. Results of numerical propagation studies show that the exact nonlinear synchronous model is consistent for both large and small time steps, though numerical issues exist for very small time steps. Comparison with reference propagations shows that the synchronous element exact dynamic model is as accurate as Keplerian and Cartesian propagations and is therefore suitable for precise dynamic modeling. The small-inclination model is as accurate as the exact model for inclinations less than 1 deg. However, the small-eccentricity linearized model is accurate only to the order of tens of meters.

A hybrid set of modified equinoctial elements is chosen and a reduced dynamic model used to batch process multiple nights of experimental optical data of the Tracking and Data Relay Satellite (TDRS) 8. The hybrid element estimator performance is compared to that of an inertial Cartesian state estimator, which uses identical dynamic and measurement models. Comparison to the NASA Goddard Space Flight Center Flight Dynamics Facility (FDF) osculating element sets shows that the hybrid estimator is able to capture the in-track position and radial velocity of the orbit significantly better than the inertial Cartesian estimator (hundreds of meters in position and a few centimeters per second in velocity). Reference residuals indicate a declination bias of approximately 1 arcsecond and a subarcsecond time-varying right ascension offset, which may account for approximately 200 m of position error. Simulation studies, conducted to eliminate the presence of mismodeled dynamics and measurements, confirm that the in-track position and radial velocity estimation discrepancy between the two element sets is a direct result of the estimation process. Comparison of the estimated state uncertainties shows that the inertial Cartesian batch longitudinal uncertainty is approximately 1 km larger than the hybrid longitudinal uncertainty. The batch performance discrepancy is due to the linearization of the azimuth and elevation measurement sensitivity matrix. The results of this work demonstrate that the hybrid element set is an appropriate choice for the dynamic modeling of geosynchronous satellites.

The hybrid elements may be used in a variety of ways to enhance object tracking and prediction. The strength of this element set lies in the small elemental changes for perturbed geosynchronous satellite motion. Because of the scale of the natural variations, the hybrid elements are ideal for identifying vehicle maneuvers and validating data association with metric observations.

Further work is necessary in the long-term prediction of geosynchronous satellite motion, particularly for the case of debris and other inactive satellites. Additionally, the equations of motion could be augmented to include impulsive feedback control strategies, which could then be applied to the control of multiple clustered spacecraft. The utility of the hybrid elements to data association and maneuver detection should also be investigated.

Appendix: Derivation of Exact Nonlinear Synchronous Element Variational Equations

This Appendix presents a detailed derivation of the exact nonlinear synchronous element variational equations using the method of Poisson brackets [Eq. (2)]. The derivation follows the method presented in [6,9].

I. Derivation of $\Delta\bar{a}$ Variational Equation

As $\Delta\bar{a}$ does not vary under Keplerian dynamics, only the disturbing acceleration portion of the Poisson bracket contributes to the $\Delta\bar{a}$ dynamic equation. The derivation of the exact dynamic equation for the $\Delta\bar{a}$ synchronous element begins with the vis-viva orbital energy equation, given by

$$\mathbf{v}^T\mathbf{v} = \frac{2\mu}{r} - \frac{\mu}{A(\Delta\bar{a}+1)} \tag{A1}$$

where μ is the central body gravitational parameter and $\mathbf{v}$ is the satellite velocity vector. Note that $\mathbf{v}$ is not assigned a coordinate frame. The coordinate-frame-independent variation of $\Delta\bar{a}$ with respect to the velocity vector is given by

$$\frac{\partial\Delta\bar{a}}{\partial\mathbf{v}} = \frac{2A\mathbf{v}^T}{\mu}(\Delta\bar{a}^2+1) \tag{A2}$$

A reference frame is assigned to Eq. (A2) through the definition of the velocity vector components. The position vector is defined in the rotating $[\hat{i}_r, \hat{i}_\theta, \hat{i}_h]$ local-vertical/local-horizontal (LVLH) frame by

$$\mathbf{r} = r\hat{i}_r \tag{A3}$$

The inertial time derivative of Eq. (A3) is given by

$$\dot{\mathbf{r}} = \dot{r}\hat{i}_r + r\dot{\nu}\hat{i}_\theta \tag{A4}$$

where $\dot{\nu}$ denotes the time derivative of the true anomaly. The orbit equation and angular momentum magnitude are given by

$$r = \frac{h^2}{\mu[1+e\cos(\nu)]} \tag{A5}$$

$$h = r^2\dot{\nu} \tag{A6}$$

Using Eqs. (A5) and (A6), the time rate of orbit radius magnitude is given by

$$\dot{r} = \frac{\mu}{h}e\sin(\nu) \tag{A7}$$

Equation (A6) is used to express the quantity $r\dot{\nu}$ as

$$r\dot{\nu} = \frac{\mu p}{hr} \tag{A8}$$

Substituting Eqs. (A7) and (A8) into Eq. (A4) allows the velocity vector to be expressed in the LVLH frame as

$$\mathbf{v} = \dot{\mathbf{r}} = \frac{\mu}{h}\left[(e_x \sin(s) - e_y \cos(s))\hat{i}_r + \frac{p}{r}\hat{i}_\theta\right] \tag{A9}$$

Substituting Eq. (A9) into Eq. (A2) gives the LVLH frame partial derivative of $\Delta\bar{a}$ with respect to velocity as

$$\frac{\partial \Delta\bar{a}}{\partial \mathbf{v}} = \frac{2(\Delta\bar{a}+1)^2}{Ah}\left[(e_x \sin(s) - e_y \cos(s))\hat{i}_r + \frac{p}{r}\hat{i}_\theta\right] \tag{A10}$$

The disturbing acceleration vector is defined in the LVLH frame as

$$\mathbf{a}_D = [\,a_r \quad a_\theta \quad a_h\,] \tag{A11}$$

Finally, multiplying Eq. (A10) by the disturbing acceleration vector gives the perturbed time rate of change of $\Delta\bar{a}$ as

$$\Delta\dot{\bar{a}} = \frac{2A(\Delta\bar{a}+1)^2}{h}\left[(e_x \sin(s) - e_y \cos(s))a_r + \frac{p}{r}a_\theta\right] \tag{A12}$$

II. Derivation of i_x and i_y Variational Equations

As the i_x and i_y synchronous elements do not vary under Keplerian motion, their motion is a function of only the perturbing accelerations. The angular momentum vector expressed in the orbit-fixed $[\hat{i}_n, \hat{i}_m, \hat{i}_h]$ reference frame is given by

$$\mathbf{h} = h\hat{i}_h \tag{A13}$$

The orbit frame is defined by the direction of perigee $\hat{i}_n$, orbit normal $\hat{i}_h$, and the completion of the right-hand orthogonal frame $\hat{i}_m$. The direction cosine matrix to rotate from the inertial $[\hat{i}_i, \hat{i}_j, \hat{i}_k]$ frame to the orbit frame is given by

$$\begin{pmatrix}\hat{i}_n\\ \hat{i}_m\\ \hat{i}_h\end{pmatrix} = \begin{bmatrix} -i_y i^{-1} & i_x i^{-1} & 0\\ -i_x\cos(i)i^{-1} & -i_y\cos(i)i^{-1} & \sin(i)\\ i_x\sin(i)i^{-1} & i_y\sin(i)i^{-1} & \cos(i)\end{bmatrix}\begin{pmatrix}\hat{i}_i\\ \hat{i}_j\\ \hat{i}_k\end{pmatrix} \tag{A14}$$

This rotation matrix is used to express the angular momentum vector is terms of i_x and i_y as

$$\mathbf{h} = h\hat{i}_h = h[i_x \sin(i)i^{-1}\hat{i}_i + i_y \sin(i)i^{-1}\hat{i}_j + \cos(i)\hat{i}_k] \tag{A15}$$

The partial derivatives of i_x and i_y with respect to the velocity vector are determined by manipulating Eq. (A15). The partial derivative of Eq. (A15) is broken down into the contributions from h, i_x, and i_y as

$$\frac{\partial \mathbf{h}}{\partial \mathbf{v}} = \frac{\partial \mathbf{h}}{\partial h}\frac{\partial h}{\partial \mathbf{v}} + \frac{\partial \mathbf{h}}{\partial i_x}\frac{\partial i_x}{\partial \mathbf{v}} + \frac{\partial \mathbf{h}}{\partial i_y}\frac{\partial i_y}{\partial \mathbf{v}} \tag{A16}$$

Expanding the right side of Eq. (A16) produces

$$\begin{aligned}\frac{\partial \mathbf{h}}{\partial \mathbf{v}} = &\left[\frac{i_x \sin(i)}{i}\hat{i}_i + \frac{i_y \sin(i)}{i}\hat{i}_j + \cos(i)\hat{i}_k\right]\frac{\partial h}{\partial \mathbf{v}}\\ &+ h\left[\left(\frac{i_x^2\cos(i)}{i^2} + \frac{i_y^2\sin(i)}{i^3}\right)\hat{i}_i + \left(\frac{i_x i_y\cos(i)}{i^2} - \frac{i_x i_y \sin(i)}{i^3}\right)\hat{i}_j\right.\\ &\left. - \frac{i_x\sin(i)}{i}\hat{i}_k\right]\frac{\partial i_x}{\partial \mathbf{v}} + h\left[\left(\frac{i_x i_y\cos(i)}{i^2} - \frac{i_x i_y\sin(i)}{i^3}\right)\hat{i}_i\right.\\ &\left. + \left(\frac{i_y^2\cos(i)}{i^2} + \frac{i_x^2\sin(i)}{i^3}bigg\right)\hat{i}_j - \frac{i_y\sin(i)}{i}\hat{i}_k\right]\frac{\partial i_y}{\partial \mathbf{v}}\end{aligned} \tag{A17}$$

The velocity partial derivative of the angular momentum vector is also given by

$$\frac{\partial \mathbf{h}}{\partial \mathbf{v}} = \frac{\partial(\mathbf{r}\times\mathbf{v})}{\partial \mathbf{v}} = (\mathbf{r}\times) \tag{A18}$$

Additionally, the satellite position vector is expressed in orbit frame components as

$$\mathbf{r} = r(\cos(s-\Omega)\hat{i}_n + \sin(s-\Omega)\hat{i}_m) \tag{A19}$$

Equation (A19) is substituted into Eq. (A18), and the result is set equal to Eq. (A17). Next, the inertial frame unit vectors are expressed in orbit frame components using Eq. (A14). Though the resulting equation is quite algebraically complex, respective multiplication by the $\hat{i}_n$ and $\hat{i}_m$ unit vectors isolates the orbit frame components and provides two independent equations that are functions of $\partial i_x/\partial \mathbf{v}$ and $\partial i_y/\partial \mathbf{v}$. The partial derivates are then solved algebraically as

$$\frac{\partial i_x}{\partial \mathbf{v}} = \left[\frac{r}{h}\sin(\Omega)\cos(\omega+\nu) + \frac{ir}{h\sin(i)}\cos(\Omega)\sin(\omega+\nu)\right]\hat{i}_h \tag{A20}$$

$$\frac{\partial i_y}{\partial \mathbf{v}} = \left[\frac{ir}{h\sin(i)}\sin(\Omega)\sin(\omega+\nu) - \frac{r}{h}\cos(\Omega)\cos(\omega+\nu)\right]\hat{i}_h \tag{A21}$$

Multiplication by the LVLH frame disturbing acceleration vector completes the Poisson bracket derivation of the exact nonlinear i_x and i_y variational equations, given by

$$\dot{i}_x = \left[\frac{r}{h}\sin(\Omega)\cos(\omega+\nu) + \frac{ir}{h\sin(i)}\cos(\Omega)\sin(\omega+\nu)\right]a_h \tag{A22}$$

$$\dot{i}_y = \left[\frac{ir}{h\sin(i)}\sin(\Omega)\sin(\omega+\nu) - \frac{r}{h}\cos(\Omega)\cos(\omega+\nu)\right]a_h \tag{A23}$$

III. Derivation of e_x and e_y Dynamic Equations

The eccentricity synchronous elements are only varied through orbit perturbations. To begin the Poisson bracket derivation of the variational equations, the angular momentum magnitude is expressed as

$$h^2 = r^2\mathbf{v}^T\mathbf{v} - (\mathbf{r}^T\mathbf{v})^2 \tag{A24}$$

The partial derivative of Eq. (A24) with respect to the velocity vector is given by

$$\frac{\partial h}{\partial \mathbf{v}} = r^2\mathbf{v}^T - (\mathbf{r}^T\mathbf{v})\mathbf{r}^T \tag{A25}$$

The angular momentum magnitude can also be expressed in terms of the synchronous elements as

$$h^2 = A\mu(\Delta\bar{a}+1)(1-e_x^2-e_y^2) \tag{A26}$$

The partial derivative of Eq. (A26), using Eq. (A10), is given by

$$\begin{aligned}\frac{\partial h}{\partial \mathbf{v}} = -2a\mu\Bigg(&e_x\frac{\partial e_x}{\partial \mathbf{v}} + e_y\frac{\partial e_y}{\partial \mathbf{v}} - \frac{a(1-e_x^2-e_y^2)}{2h}\\ &\times\left[(e_x\sin(s) - e_y\cos(s))\hat{i}_r + \frac{p}{r}\hat{i}_\theta\right]\Bigg)\end{aligned} \tag{A27}$$

Setting Eq. (A25) equal to Eq. (A27) provides one algebraic equation in terms of the two unknown partial derivatives, $\partial e_x/\partial \mathbf{v}$ and $\partial e_y/\partial \mathbf{v}$.

A second equation in terms of both partial derivatives is necessary. The partial derivative of the orbit equation (A5) is given by

$$2h\frac{\partial h}{\partial \mathbf{v}} = r\mu\left(\cos(s)\frac{\partial e_x}{\partial \mathbf{v}} + \sin(s)\frac{\partial e_y}{\partial \mathbf{v}} + [e_y\cos(s) - e_x\sin(s)]\frac{\partial s}{\partial \mathbf{v}}\right) \tag{A28}$$

Using the definition of s [Eq. (1g)] and the partial derivatives of the Keplerian elements ν, Ω, and ω presented in [9], the partial derivative of the sidereal angle is given by

$$\frac{\partial s}{\partial \mathbf{v}} = \frac{\partial \Omega}{\partial \mathbf{v}} + \frac{\partial \omega}{\partial \mathbf{v}} + \frac{\partial \nu}{\partial \mathbf{v}} = [1 - \cos(i)] \frac{r \sin(\theta)}{h \sin i} \hat{i}_h \tag{A29}$$

Substituting Eq. (A29) and Eq. (A25) into Eq. (A28) provides a second independent equation in terms of the e_x and e_y partial derivatives. Solving simultaneously with the first equation in terms of both unknown partial derivatives and substituting in the position and velocity vectors [Eqs. (A3) and (A9)] produces the partial derivatives of e_x and e_y with respect to the velocity vector, as given by

$$\dot{e}_x = \frac{r}{h}\left\{\frac{p}{r}\sin(s)\hat{i}_r + \left[e_x + \left(1 + \frac{p}{r}\right)\cos(s)\right]\hat{i}_\theta\right\} + e_y \frac{r}{h}\left\{\left[\tan\left(\frac{i}{2}\right)\sin(\Omega)\cos(s) - \tan\left(\frac{i}{2}\right)\cos(\Omega)\sin(s)\right]\hat{i}_h\right\} \tag{A30}$$

$$\dot{e}_y = \frac{r}{h}\left\{\frac{-p}{r}\cos(s)\hat{i}_r + \left[e_y + \left(1 + \frac{p}{r}\right)\sin(s)\right]\hat{i}_\theta\right\} - e_x \frac{r}{h}\left\{\left[\tan\left(\frac{i}{2}\right)\sin(\Omega)\cos(s) - \tan\left(\frac{i}{2}\right)\cos(\Omega)\sin(s)\right]\hat{i}_h\right\} \tag{A31}$$

To complete the derivation of the variational equations, Eqs. (A30) and (A31) are multiplied by the disturbing acceleration vector [Equation (A11)]. The resulting exact nonlinear variational equations are given by

$$\dot{e}_x = \frac{r}{h}\left\{\frac{p}{r}\sin(s)a_r + \left[e_x + \left(1 + \frac{p}{r}\right)\cos(s)\right]a_\theta\right\} + e_y \frac{r}{h}\left\{\left[\tan\left(\frac{i}{2}\right)\sin(\Omega)\cos(s) - \tan\left(\frac{i}{2}\right)\cos(\Omega)\sin(s)\right]a_h\right\} \tag{A32}$$

$$\dot{e}_y = \frac{r}{h}\left\{\frac{-p}{r}\cos(s)a_r + \left[e_y + \left(1 + \frac{p}{r}\right)\sin(s)\right]a_\theta\right\} - e_x \frac{r}{h}\left\{\left[\tan\left(\frac{i}{2}\right)\sin(\Omega)\cos(s) - \tan\left(\frac{i}{2}\right)\cos(\Omega)\sin(s)\right]a_h\right\} \tag{A33}$$

IV. Derivation of λ Dynamic Equation

The longitude synchronous element, λ, varies both naturally and under orbit perturbations. As such, the λ variational equation is defined as

$$\frac{\mathrm{d}\lambda}{\mathrm{d}t} = \frac{\partial \lambda}{\partial \mathbf{v}}\mathbf{a}_D + \frac{\partial \lambda}{\partial t} \tag{A34}$$

The definition of λ [Eq. (1a)] is differentiated with respect to time to produce

$$\frac{\partial \lambda}{\partial t} = \frac{\partial s}{\partial t} - \frac{\partial G(t)}{\partial t} \tag{A35}$$

The time derivative of the Greenwich angle is simply the rotation rate of the Earth, ω_E. The time partial derivative of the sidereal angle is computed by differentiating the sidereal-angle definition [Eq. (1g)] and substituting the Keplerian element time partial derivatives presented in [9]. The sidereal-angle time partial derivative is given by

$$\frac{\partial s}{\partial t} = \frac{\partial \Omega}{\partial t} + \frac{\partial \omega}{\partial t} + \frac{\partial \nu}{\partial t} = \frac{h}{r^2} \tag{A36}$$

Substituting Eq. (A36) and the Earth rotation rate into Eq. (A37) produces the time partial derivative of λ as

$$\frac{\partial \lambda}{\partial t} = \frac{h}{r^2} - \omega_E \tag{A37}$$

Using Eq. (A29) and the definition of λ, the velocity vector partial derivative of λ is given by

$$\frac{\partial \lambda}{\partial \mathbf{v}} = \frac{\partial s}{\partial \mathbf{v}} = [1 - \cos(i)] \frac{r \sin(\theta)}{h \sin i} \hat{i}_h \tag{A38}$$

Substituting Eqs. (A37), (A38), and (A11) into Eq. (A34), the exact variational equation of λ is given by

$$\dot{\lambda} = \frac{h}{r^2} + \frac{r}{h}\tan\left(\frac{i}{2}\right)\sin(\omega + \nu)a_h - \Omega_E \tag{A39}$$

Acknowledgments

The authors would like to thank the U.S. Air Force Maui Optical and Supercomputing Site for providing both data and technical support throughout this project. This work was funded by the National Defense Science and Engineering Graduate Fellowship. This paper was cleared for public release by the U.S. Air Force Research Laboratory on 29 December 2009 (case number 377ABW-2009-1626).

References

[1] Jehn, R., Agapov, V., and Hernandez, C., "The Situation in the Geostationary Ring," *Advances in Space Research*, Vol. 35, March 2005, pp. 1318–1327. doi:10.1016/j.asr.2005.03.022

[2] Soop, E., *Handbook of Geostationary Orbits*, Chap. 2.3. Kluwer Academic, Dordrecht, The Netherlands, 1994.

[3] Junkins, J. L., "Adventures on the Interface of Dynamics and Control," *Journal of Guidance, Control, and Dynamics*, Vol. 20, 1997, pp. 1058–1071. doi:10.2514/2.4176

[4] Valk, S., and Lemaitre, A., "Semi-Analytical Investigations of High Area-to-Mass Ratio Geosynchronous Space Debris Including Earth's Shadowing Effects," *Advances in Space Research*, Vol. 42, 2008, pp. 1429–1443. doi:10.1016/j.asr.2008.02.010

[5] Valk, S., Lemaitre, A., and Deleflie, F., "Semi-Analytical Theory of Mean Orbital Motion for Geosynchronous Space Debris Under Gravitational Influence," *Advances in Space Research*, Vol. 43, 2009, pp. 1070–1082. doi:10.1016/j.asr.2008.12.015

[6] Battin, R., *An Introduction to the Mathematics and Methods of Astrodynamics*, AIAA, New York, 1999, Chap. 10.5.

[7] Sidi, M. J., *Spacecraft Dynamics and Control: A Practical Engineering Approach*, Cambridge Univ. Press, Cambridge, England, U.K., 1997, Chap. 2.7.

[8] Alby, F., *The Motion of Satellite, Lectures and Exercises on Space Mechanics*, Cepadues-Editions, Toulouse, France, 1983, pp. 569–611.

[9] Schaub, H., and Junkins, J. L., *Analytical Mechanics of Space Systems*, AIAA, Reston, VA, 2003, pp. 511–522.

[10] Julier, S. J., and Uhlmann, J. K., "A New Extension of the Kalman Filter to Nonlinear Systems," *Proceedings of SPIE*, Vol. 3068, 1997, pp. 182–193. doi:10.1117/12.280797